Nano Research

Open Access

Research Article

Single atom Cu-O_2N bridge between $BiVO_4$ and COFs toward photoelectrochemical seawater splitting

Zicong Zhang, Gaohang Song, Wenming Sun ✉, Zhaorui Hua, and Yang Tian ✉

Department of Chemistry, Capital Normal University, Beijing 100048, China

Cite this article: *Nano Research*, **2025**, *18*, 94907273. https://doi.org/10.26599/NR.2025.94907273

ABSTRACT: Photoelectrochemical (PEC) water splitting has great potential for solar energy conversion to hydrogen. However, the slow charge transfer in the photoanodes remains a core issue limiting the PEC performance. In this study, we address this issue by constructing a single-atom bridge (SAB) Cu-O_2N at the interface between $BiVO_4$ and covalent organic framework (COF) layer. X-ray absorption fine spectra and theoretical calculations demonstrate that the single-atom bridge is formed by the interfacial coordination reconstruction between $BiVO_4$ and COF layers and create intermediate electronic states to facilitate the hole extraction. As a result, the SAB photoanode exhibits enhanced PEC water oxidation performance. Specifically, it achieves a photocurrent density of 4.84 mA·cm^{-2} at 1.23 V vs. reversible hydrogen electrode (RHE) in PEC simulant seawater splitting with a cocatalyst, higher than nearly all the previously reported $BiVO_4$-based photoanodes. This work offers valuable insights into fast charge transfer in PEC systems and proposes a promising strategy for designing efficient photoelectrodes for seawater splitting.

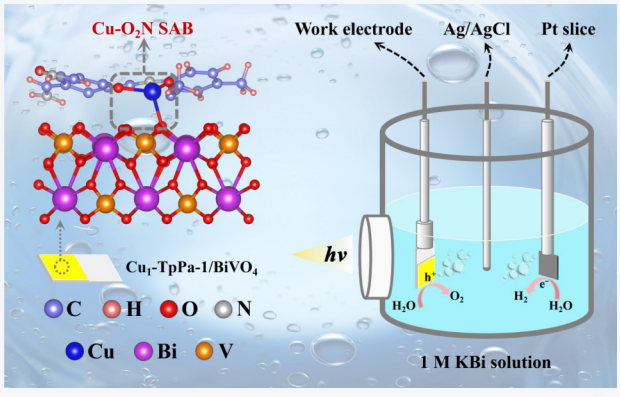

KEYWORDS: single-atom bridge, photoelectrochemical, seawater splitting

1 Instructions

As a sustainable technology, photoelectrochemical (PEC) water splitting has gained wide attention in solving energy and environmental issues by converting the solar energy into hydrogen energy [1–8]. However, one of the major challenges in achieving efficient PEC water splitting is the sluggish oxygen evolution reaction (OER) at the photoanode [9–13]. Achieving efficient PEC water splitting relies on the development of semiconductor photoanodes, which are already available for PEC water splitting, such as Fe_2O_3, TiO_2, and $BiVO_4$ [14–17]. Unfortunately, the photogenerated carriers usually recombine rapidly in these semiconductors, resulting in photocurrent densities that are significantly lower than the theoretical values, and so the PEC performance is severely limited [18–22]. Therefore, exploring effective charge transport channel that can rapidly transfer charge out of the semiconductor is currently anticipated in PEC water splitting.

Single-atom bridge (SAB) is a type of charge transport channel that connects distinct materials by using single atoms [23–26]. With suitable electron affinity, single atoms acting as transport medium can effectively exchange the charges with other materials, reducing the resistance to accelerate the charge transport and charge separation [27–30]. At the same time, the flexible coordination environment of single atoms is favorable to modulate the charge transfer behavior of SAB. Recently, Wang et al. designed a N–Cu_1–S single-atom electron bridge to prompt a Z-scheme photocatalyst with excellent performance in CO_2 reduction [23]. However, isolating a single atom as a bridge is still a challenge due to that the aggregates or clusters may form [31–33]. Covalent organic frameworks (COFs) have emerged as promising support for metal single atoms due to facilitating the incorporation of specific binding sites that can strongly coordinate metal atoms [34–36]. This strong coordination is crucial for stabilizing the metal atoms, thereby impeding their aggregates [37–40]. Additionally, COFs exhibit excellent electrical conductivity due to strong transverse π-orbital conjugation between neighboring layers and inherent π–π interactions, making them an excellent choice for

Received: December 2, 2024; **Revised:** January 18, 2025
Accepted: January 24, 2025

✉Address correspondence to Wenming Sun, swm@mail.sdu.edu.cn; Yang Tian, tianyang@cnu.edu.cn

charge transport layers [41–43]. Therefore, constructing covalent SAB between the COFs and semiconductor surface in PEC device to improve the interfacial carrier dynamics is highly desired, but has rarely been reported [29].

$BiVO_4$ has emerged as one of the most promising photoanode materials for PEC water splitting due to its favorable bandgap (2.4 eV) and high theoretical photocurrent. Recent advancements in $BiVO_4$ photoanodes have significantly enhanced their performance in PEC water splitting, driven by strategies such as heterojunction engineering, doping, and surface modification [12, 14, 15]. For instance, Chen's group reported $BiVO_4$ photoanodes achieving a photocurrent density as high as 7.01 $mA{\cdot}cm^{-2}$ for PEC water oxidation [44]. Despite these improvements, challenges such as charge recombination and long-term stability remain, particularly in the context of seawater splitting. When the $BiVO_4$ photoanodes are used for PEC seawater splitting, the photoelectric response exceeding 4.5 $mA{\cdot}cm^{-2}$ with long-term stability is still rarely reported. Ongoing research is needed to develop highly efficient and durable $BiVO_4$-based photoanodes to enable solar hydrogen production from seawater.

In this work, we prepared an SAB Cu-O_2N supported by the TpPa-1, one of the typical COF materials, that can transfer the charge out of $BiVO_4$ photoanode. X-ray absorption fine spectra and theoretical calculations illustrate that the coordination environment of Cu single-atoms is reconstructed upon the formation of the stable interface of TpPa-1 with $BiVO_4$ through SAB. The Cu single-atom is coordinated with O and N atoms at the interface of COF and $BiVO_4$, forming a covalent bridge bond. It could provide intermediate electron energy states to narrow the gap of the interface. Thereby, it builds a channel facilitating charge transfer from the $BiVO_4$ semiconductor to the COF. As expected, it promoted the PEC performance for water splitting, especially for simulated seawater (SSW) splitting. Notably, its photocurrent density reaches 4.84 $mA{\cdot}cm^{-2}$ in simulated seawater at 1.23 V vs. reversible hydrogen electrode (RHE) with a co-catalyst. Moreover, it shows long-term stability in SSW for more than 60 h of illumination. This study demonstrates the significant enhancement of PEC water oxidation performance through incorporating Cu-O_2N SAB with COF supports, provides a promising strategy for the design of efficient and stable seawater splitting photoanodes.

2 Results and discussion

The $BiVO_4$ substrate on fluorine-doped tin oxide (FTO) was synthesized according to a previously reported work [42]. The COF of TpPa-1 was prepared by mechanical milling method [43]. Subsequently, the TpPa-1 was loaded with Cu single-atoms by adding it to copper acetate (Ac) solution, obtaining the powder of pristine Cu_1-TpPa-1 [38]. Finally, the Cu_1-TpPa-1 was deposited on the $BiVO_4$ substrate by a solvothermal method, achieving the product of Cu_1-TpPa-1/$BiVO_4$ in Fig. 1(a). For comparison, the TpPa-1 located on $BiVO_4$ without Cu atom was also prepared, named TpPa-1/$BiVO_4$. The detailed preparation methods are present in experimental section.

The prepared Cu_1-TpPa-1/$BiVO_4$ were observed by scanning electronic microscopy (SEM) for micro-morphology. Figure 1(b) shows that $BiVO_4$ deposited on FTO glass is composed of worm-like porous nanoparticles in 200 nm width and 2 μm length, agreement with that of reference reported [10, 14, 15, 45]. Meanwhile, the loading of Cu_1-TpPa-1 has no significant effect on the basic morphology of $BiVO_4$ (Fig. S1 in the Electronic Supplementary Material (ESM)). In Fig. 1(c), the lattice spacing of 0.25 nm corresponding to the (002) facet of $BiVO_4$ can be seen from the high-resolution transmission electron microscopy (HRTEM) images. A distinct interface between the $BiVO_4$ semiconductor and Cu_1-TpPa-1 can be observed, indicating that the $BiVO_4$ nanocrystals are tightly wrapped by the Cu_1-TpPa-1. The high-angle annular dark-field scanning TEM (HAADF-STEM) image further reveals the atomic-level dispersion of Cu species in the Cu_1-TpPa-1/$BiVO_4$ as shown in Fig. 1(d) and Fig. S5 in the ESM. The elemental distribution of Bi, V, O, C, N, and Cu in the Cu_1-TpPa-1/$BiVO_4$ was verified by energy dispersive spectrometer (EDS) mapping (Fig. 1(e) and Fig. S6 in the ESM). The inductively coupled plasma-mass spectrometry (ICP-MS) was used to further determine the Cu content as 2.75 wt.% in Cu_1-TpPa-1.

The crystal structures of Cu_1-TpPa-1/$BiVO_4$ product were characterized by X-ray diffraction (XRD) compared with $BiVO_4$, TpPa-1, and TpPa-1/$BiVO_4$ (Fig. 1(f) and Figs. S1(c) and S1(d) in the ESM). In addition to the detection of characteristic peaks belonging to the $BiVO_4$ (JCPDS No. 14-0688), three characteristic peaks of TpPa-1 were detected at 4.7°, 8.1°, and 27° corresponding to the (100), (200) and (001) crystal planes [37], which demonstrates the effective fabrication of TpPa-1 loading on $BiVO_4$. To further indicate the presence of COF in the Cu_1-TpPa-1/$BiVO_4$ product, we performed the Fourier transform infrared spectra (FT-IR) in contrast to $BiVO_4$, TpPa-1, and TpPa-1/$BiVO_4$ (Figs. 1(g) and 1(h)). The peaks at 1582 and 1255 cm^{-1} are corresponded to the C=O stretching vibration peaks and C–N stretching vibration peaks [37, 38, 46], respectively. The appearance of the C=O stretching vibrational peak indicates the success of an irreversible enol-keto tautomerization reaction, which effectively demonstrates the successful synthesis of TpPa-1. The Raman spectroscopy studies confirmed that both the TpPa-1/$BiVO_4$ and Cu_1-TpPa-1/$BiVO_4$ contained characteristic peaks of TpPa-1 and $BiVO_4$ (Fig. S7 in the ESM).

To obtain the detailed atomic structure information for the Cu-O_2N SAB in Cu_1-TpPa-1/$BiVO_4$, we performed measurements of X-ray absorption near-edge structure (XANES) spectroscopy and extended X-ray absorption fine structure (EXAFS) spectra. The XANES in Fig. 2(a) determines the oxidation state of Cu in the Cu_1-TpPa-1/$BiVO_4$ around +2 compared with the standard CuO and copper phthalocyanine (CuPc). Moreover, in the local enlarged view (the inset of Fig. 2(a)), the oxidation state of Cu in the Cu_1-TpPa-1/$BiVO_4$ (purple line) shifts higher than it in pristine Cu_1-TpPa-1 sample (black line), indicating a potential covalent interaction between the Cu single atom with the $BiVO_4$ after the Cu_1-TpPa-1 loading on the $BiVO_4$.

The EXAFS of Cu element (Fig. 2(b)) displays the main peak of pristine Cu_1-TpPa-1 sample locates at 1.43 Å in the *R*-space, which corresponds to the Cu–N bond or Cu–O bond. Meanwhile, the Cu–Cu coordination peak at 2.2 Å disappears at the corresponding position in Cu_1-TpPa-1. These demonstrate well that the Cu atoms atomically dispersing with the coordination of N and O. The EXAFS fitting in Fig. 2(c) and Fig. S8(a) in the ESM show that the Cu single-atoms in pristine Cu_1-TpPa-1 is coordinated with one N atom and three O atoms (Table S2 in the ESM), which belongs to the TpPa-1 COF and acetate molecule as shown in Fig. 2(e). This structure result is in good accord with the loading of Cu single-atoms on TpPa-1 as previously reported [38].

In contrast, after the Cu_1-TpPa-1 loading on the $BiVO_4$, the main

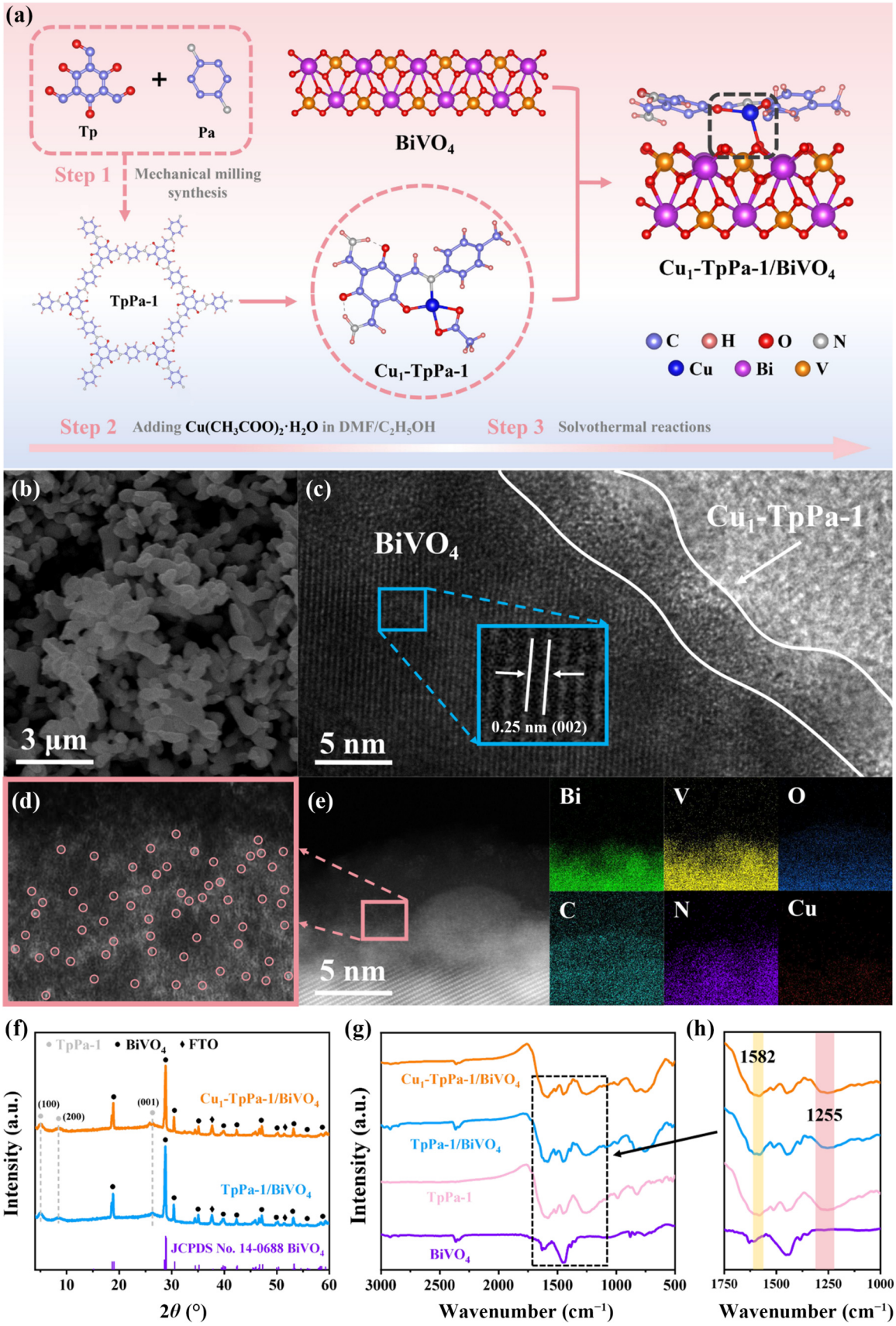

Figure 1 (a) Schematic illustration of the synthesis process. (b) SEM image of $BiVO_4$. (c) HRTEM image of Cu_1-TpPa-1/$BiVO_4$. (d) HAADF-STEM image of Cu_1-TpPa-1/$BiVO_4$. (e) EDS mapping of Cu_1-TpPa-1/$BiVO_4$. (f) XRD patterns of TpPa-1/$BiVO_4$ and Cu_1-TpPa-1/$BiVO_4$. (g) FT-IR spectra of $BiVO_4$, TpPa-1, TpPa-1/$BiVO_4$ and Cu_1-TpPa-1/$BiVO_4$ and (h) local magnification of FT-IR spectra in the wavenumber range 1000 to 1750 as marked in (g).

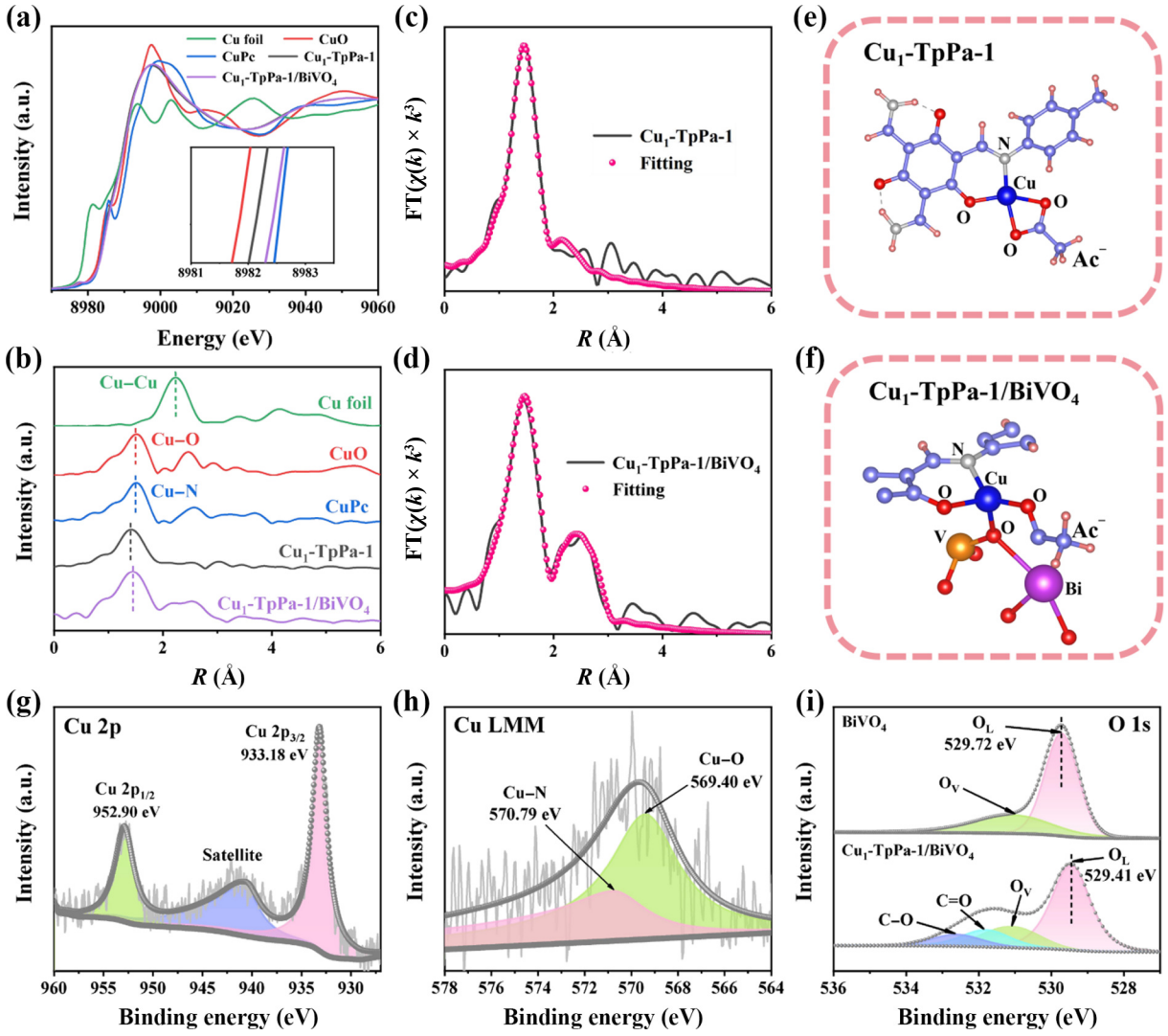

Figure 2 (a) Cu K-edge XANES spectra. (b) Cu K-edge EXAFS spectra. (c) and (d) EXAFS fitting spectra. (e) and (f) Coordination structure of Cu single-atom bridge. (g) High-resolution XPS spectrum for the Cu 2p of Cu_1-TpPa-1/$BiVO_4$. (h) The Auger spectrum for the Cu LMM of Cu_1-TpPa-1/$BiVO_4$. (i) High-resolution XPS spectra for O 1s of $BiVO_4$ and Cu_1-TpPa-1/$BiVO_4$.

peak (or the first-shell coordination peak) shifts right a little compared with that of pristine Cu_1-TpPa-1, indicating the longer covalent bonds of Cu–O and Cu–N caused by the interaction between the Cu atom with $BiVO_4$. More importantly, a second-shell coordination peak around 2.51 Å appears after the Cu_1-TpPa-1 loading on the $BiVO_4$. The EXAFS fitting (Fig. 2(d) and Fig. S8(b) in the ESM) combined with density functional theory (DFT) calculation (Fig. 2(f)) suggest that the second-shell coordination peak is attributed to the Cu–O–V scattering path. Therefore, the Cu single-atom coordination in the Cu_1-TpPa-1 is reconstructed when it loads on the $BiVO_4$ for the Cu_1-TpPa-1/$BiVO_4$. The reasonable local coordination structure could be deduced in Fig. 2(f): Excepting the coordination with one N and one O atom in TpPa-1 and one O atom in acetate, a new covalent bridge bond between the Cu atom (in Cu_1-TpPa-1) and the O atom (in $BiVO_4$) forms. Evidently, the Cu-O_2N SAB is constructed at the interface between the $BiVO_4$ and the COF layer of TpPa-1.

X-ray photoelectron spectroscopy (XPS) measurements were used to gain further insight into the chemical information about the samples (Figs. 2(g)–2(i) and Fig. S9 in the ESM). The high-resolution XPS spectrum of Cu 2p (Fig. 2(g)) indicates the presence of Cu in the form of Cu^{2+} in Cu_1-TpPa-1/$BiVO_4$, in accordance with the XANES result. In addition, the accompanying Auger peaks (Cu LMM, L and M represent electron shells involved in the emission process) at 569.40 and 570.79 eV (Fig. 2(h)) are attributed to the binding energies of the Cu–O and Cu–N bonds in Cu_1-TpPa-1/$BiVO_4$ [23, 47], respectively. Figure 2(i) shows the high-resolution XPS spectra of O 1s in $BiVO_4$ and Cu_1-TpPa-1/$BiVO_4$, in which the binding energy of lattice O of $BiVO_4$ shift lower after the $BiVO_4$ was located with Cu_1-TpPa-1 [23, 48]. The lower binding energy validates well that the surface O atoms at $BiVO_4$ accept electrons from Cu_1-TpPa-1 via covalent bonds.

The interfacial structure of the Cu_1-TpPa-1/$BiVO_4$ was then investigated and compared with TpPa-1/$BiVO_4$ by using experiments assisted by DFT calculations. Firstly, based on the experimental tests of ultraviolet–visible (UV–vis) spectra and ultraviolet photoelectron spectroscopy (UPS) analysis (Fig. S10 in the ESM), the energy band structures of the Cu_1-TpPa-1 and $BiVO_4$ are depicted in Fig. S10(f) in the ESM. It was found that the conduction band (CB) of Cu_1-TpPa-1 (−3.98 eV) meets the thermodynamic requirements for the standard potential of $O_2/\cdot O_2^-$ (−4.17 eV) [11], whereas the CB of $BiVO_4$ (−4.21 eV) does not [46,

49, 50]. To determine the energy band structure after the two composites combined, electron paramagnetic resonance (EPR) spectra were recorded using (5,5-dimethyl-l-pyrroline N-oxide (DMPO)) as a probe. Under visible light irradiation, no $\cdot O_2^-$ signal was detected for $BiVO_4$, as shown in Fig. 3(a). In contrast, a quartet of $\cdot O_2^-$ with an intensity ratio of 1:1:1:1 was observed for the Cu_1-TpPa-1, whereas no signal was detected for the Cu_1-TpPa-1/$BiVO_4$ composite. These EPR results provide evidence for the formation of a type II heterostructure of the prepared Cu_1-TpPa-1/$BiVO_4$, in which the photogenerated electrons would transfer from the CB of Cu_1-TpPa-1 to that of $BiVO_4$ and the photogenerated holes would drift in the opposite direction, as shown in Fig. 3(b).

Then, the result is confirmed by DFT calculations: the optimized structure for Cu_1-TpPa-1/$BiVO_4$ is shown in Fig. S11 in the ESM. The frontier molecular orbitals of Cu_1-TpPa-1/$BiVO_4$ are exhibited in Fig. 3(c). Clearly, the highest occupied molecular orbitals (HOMO) of Cu_1-TpPa-1/$BiVO_4$ are concentrated on the Cu_1-TpPa-1 moiety, while the lowest unoccupied molecular orbitals (LUMO) are distributed on $BiVO_4$ moiety. Theoretically, the HOMO is dominated by donor moiety while the LUMO is dominated by acceptor moiety. Hence, the distribution of frontier molecular orbitals determined its type II heterostructure feature for Cu_1-TpPa-1/$BiVO_4$. Similarly, the type II semiconductor heterostructure is also found in the TpPa-1/$BiVO_4$ sample (Fig. S12 in the ESM).

The charge transfer dynamic was further analyzed at the Cu_1-TpPa-1/$BiVO_4$ interfacial structure by DFT. The O atoms in TpPa-1 and $BiVO_4$ surface as well as the N atoms in TpPa-1 that coordinated with Cu atom are essential compositions of Cu SAB, therefore, it is necessary to analysis their electronic properties before and after the formation of SAB. The projected density of states (PDOS) of corresponding oxygen atoms are shown in Figs. 3(d) and 3(e). For the oxygen atom in $BiVO_4$ surface (O_{BiVO_4}), it binds to Cu atom directly in Cu_1-TpPa-1/$BiVO_4$. Its covalent p band increases significantly from −2.0 eV to Fermi level after the

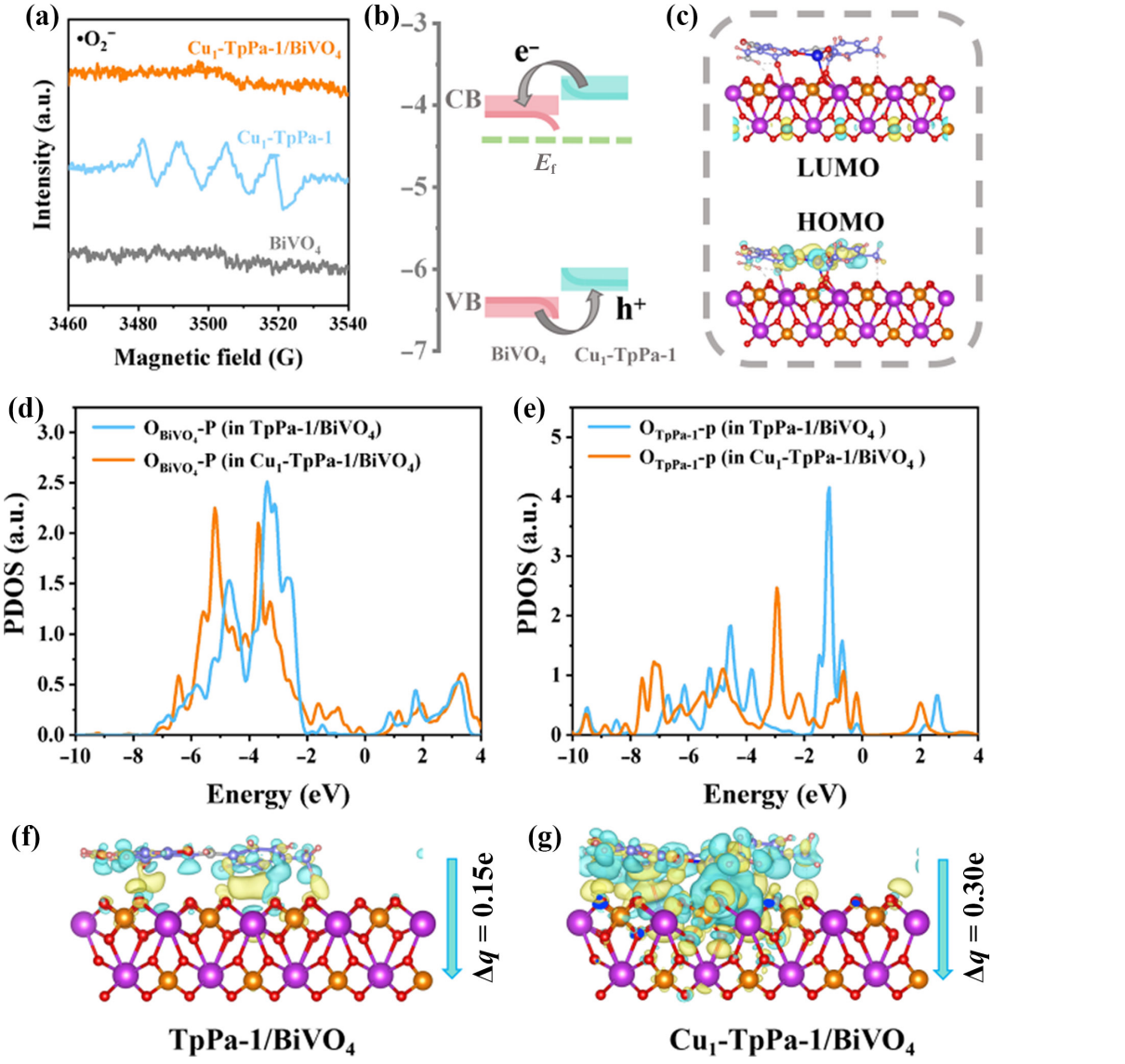

Figure 3 (a) DMPO spin-trapping EPR spectra of the $BiVO_4$, Cu_1-TpPa-1 and Cu_1-TpPa-1/$BiVO_4$. (b) Energy-band structures of Cu_1-TpPa-1/$BiVO_4$. (c) Isosurface plots of frontier orbitals for Cu_1-TpPa-1/$BiVO_4$. (d) The PDOS of O in $BiVO_4$ (comparison of loading with and without Cu single-atoms). (e) The PDOS of O in TpPa-1 and Cu_1-TpPa-1. (f) and (g) Charge difference distribution for the optimized TpPa-1/$BiVO_4$ and Cu_1-TpPa-1/$BiVO_4$ models (isosurface = 0.001 a.u.), accumulated charge in yellow and depleted charge in blue.

formation of SAB (Fig. 3(d) orange line) compared with that in the TpPa-1/$BiVO_4$ with no SAB (blue line in Fig. 3(d)). Similarly, for the oxygen atom in TpPa-1 (O_{TpPa-1}) that binds with Cu atom in the bridge, its energy edge of p conductive band (orange line in Fig. 3(e)) negatively shifts significantly relative to that of TpPa-1/$BiVO_4$ without SAB (blue line in Fig. 3(e)). Therefore, the conductivity enhancement of the p bands in both oxygen atoms connected with Cu single atom could create a channel that allows for photogenerated carrier fast transfer pathway. Similar enhancement of the PDOS near the Fermi level for the N coordinated with Cu was exhibited in Fig. S13 in the ESM, also facilitating photogenerated carrier fast transfer. Furthermore, the charge distribution of the TpPa-1/$BiVO_4$ and Cu_1-TpPa-1/$BiVO_4$ models were analyzed by Bader charge together with charge density differences. Bader charge (Δq) identifies more charge (0.30e vs. 0.15e) transferring from Cu_1-TpPa-1 into $BiVO_4$ moiety, compared with it from TpPa-1. Their charge density differences plots are depicted in Figs. 3(f) and 3(g). Significantly, more charge accumulation regions are shown yellow in $BiVO_4$ moiety for Cu_1-TpPa-1/$BiVO_4$ model. These results confirm that introducing single atomic Cu to be located at the interface of the $BiVO_4$ and TpPa-1 forming the single-atom bridge can facilitate the charge transfer and separation via the O_{BiVO_4}–Cu bridge bonds.

We then investigated the charge transport performance of the Cu_1-TpPa-1/$BiVO_4$ applied in the PEC water oxidation. Notably, we further coated the Cu_1-TpPa-1/$BiVO_4$ with an extra co-catalyst of FeOOH (named FeOOH/Cu_1-TpPa-1/$BiVO_4$), which is usually employed in PEC water splitting for the $BiVO_4$ photoanodes [5, 10, 14, 45]. Then, the prepared photoanodes were examined in a standard three-electrode system under the simulated sunlight (AM 1.5G, 100 mW·cm^{-2}), in which 1 M KBi (pH = 9.5) in pure water was used as electrolyte and Pt as counter electrode (Fig. 4(a)). The linear sweep voltammetry (LSV) curves as shown in Fig. 4(b) revealed the photocurrent density increase with the bias increasing, reaching 4.42 and 5.78 mA·cm^{-2} for the Cu_1-TpPa-1/$BiVO_4$ and FeOOH/Cu_1-TpPa-1/$BiVO_4$ at 1.23 V vs. RHE, respectively. Figure 4(c) shows the photo-electro respondence of the photoanodes under chopper light irradiation by the chronoamperometry method (20 s interval between light on and light off) at the bias of 1.23 V vs. RHE. It shows that the photocurrent density of Cu_1-TpPa-1/$BiVO_4$ increased to 4.45 mA·cm^{-2}, almost two times in contrast to TpPa-1/$BiVO_4$. Especially, with the join of FeOOH co-catalyst, the photocurrent density reaches near 6.0 mA·cm^{-2}. The applied bias photon-to-current efficiency (ABPE) of each photoanode was calculated based on the LSV curve, as shown in Fig. 4(d). It indicates the excellent

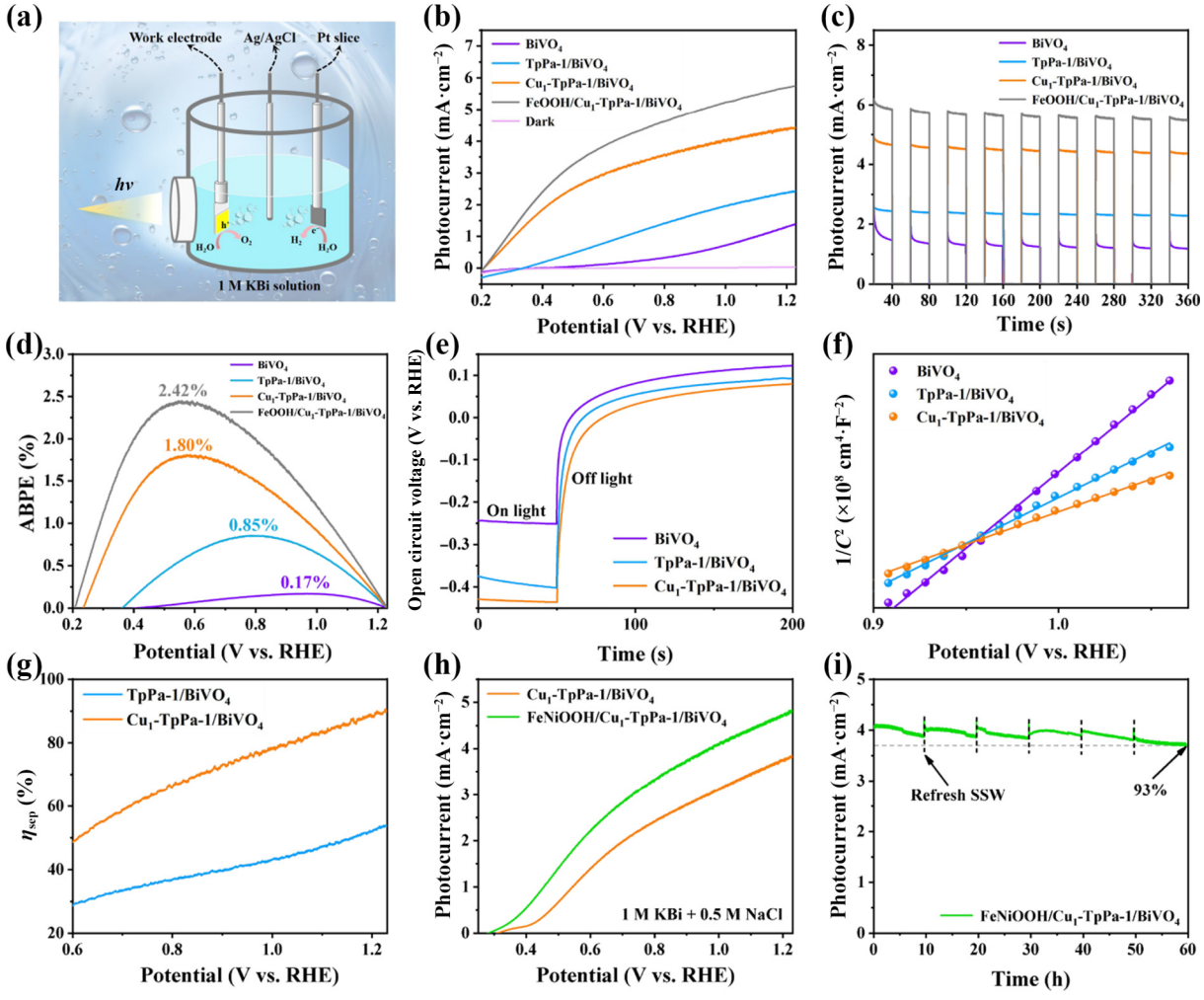

Figure 4 (a) Schematic diagram of photoelectrocatalytic water splitting device. (b) LSV curves in 1 M KBi solution. (c) Photocurrent density–time (*I*–*t*) curves in 1 M KBi solution. (d) ABPE values. (e) Open-circuit photovoltage in the dark and under irradiation. (f) Mott–Schottky plots at room temperature in dark. (g) Charge separation efficiencies. (h) LSV curves in SSW electrolytes. (i) Stability measurement for FeNiOOH/Cu_1-TpPa-1/$BiVO_4$ in SSW.

ABPE of Cu_1-TpPa-1/$BiVO_4$ was 1.80% at the low potential of around 0.6 V vs. RHE, which was 10.6 and 2.1 times higher than those of $BiVO_4$ and TpPa-1/$BiVO_4$ at higher potential. Then the ABPE reached up to 2.42% with the assistance of FeOOH co-catalyst.

The charge carrier lifetime was assessed by measuring the open-circuit photovoltages (OCP) decay (Fig. 4(e)). By comparing the decay rates of the three photoanodes, the electronic lifetimes of $BiVO_4$, TpPa-1/$BiVO_4$, and Cu_1-TpPa-1/$BiVO_4$ were calculated to be 0.069, 0.098, and 0.125 s. The results show that the longer electron lifetime indicates the faster charge transfer, which makes the electrons propagate for a longer distance, indicating the higher electron–hole separation efficiency of Cu_1-TpPa-1/$BiVO_4$. To gain insight into charge separation and transport, the Mott–Schottky (MS) curves of $BiVO_4$, TpPa-1/$BiVO_4$, and Cu_1-TpPa-1/$BiVO_4$ photoanodes were tested in the dark (Fig. 4(f)). All the photoanodes show positive slope in the MS curves, displaying the n-type characteristics. Notably, the MS curves and carrier density calculations show that the utilization of Cu single atoms as a SAB to connect TpPa-1 and $BiVO_4$ can significantly increase the charge carrier density (N_d), in which $BiVO_4$ (1.99×10^{28}) < TpPa-1/$BiVO_4$ (3.30×10^{28}) < Cu_1-TpPa-1/$BiVO_4$ (5.15×10^{28}), resulting in a preferable charge transport efficiency of Cu_1-TpPa-1/$BiVO_4$. We evaluated the charge injection efficiency (η_{inj}) and charge separation efficiency (η_{sep}) by using Na_2SO_3 as a hole scavenger (Fig. S16 in the ESM). As shown in Fig. S17 in the ESM, the charge injection efficiency at the photoanode/electrolyte interface for Cu_1-TpPa-1/$BiVO_4$ was 65.3% at 1.23 V vs. RHE, which was not significantly improved compared to that of TpPa-1/$BiVO_4$ (60.5%). In contrast, as shown in Fig. 4(g), the charge separation efficiency of Cu_1-TpPa-1/$BiVO_4$ achieved 90.3%, which was a remarkable enhancement compared to that of TpPa-1/$BiVO_4$ (53.6%). It further illustrates that a fast charge transfer channel is constructed through a Cu single atoms bridge, which can promote the rapid separation of electrons and holes in the photoanode. The detailed calculations are shown in the ESM.

To explore the potential of the prepared Cu-O_2N SAB photoanode used for PEC seawater splitting, we further studied the LSV curves and long-term stability tests of Cu_1-TpPa-1/$BiVO_4$ with FeNiOOH co-catalysts in SSW. As shown in Fig. 4(h), the Cu_1-TpPa-1/$BiVO_4$ with the co-catalysts can reach a photocurrent of 4.84 mA·cm^{-2} at 1.23 V vs. RHE in SSW, which is the highest photocurrent known for $BiVO_4$-based photoanodes in PEC seawater splitting previously reported (Table S3 in the ESM). In long-term durability measurements, the FeNiOOH/Cu_1-TpPa-1/$BiVO_4$ maintained 93% of the initial photo-response for 60 h test in SSW (refreshing SSW per 10 h) (Fig. 4(i)). The prepared photoanode structure and composition did not change significantly after the durability test in SSW by the characterization of SEM and XPS as shown in Figs. S17 and S18 in the ESM. It therefore can also be concluded that the Cu_1-TpPa-1/$BiVO_4$ stays relatively stable for a long time of persistence test with co-catalysts layer.

The charge transfer via Cu SAB between the COF and $BiVO_4$ was investigated at the excitation state by femtosecond transient absorption (fs-TA) spectroscopy. As a reference, the $BiVO_4$ shows the weak negative signals around the 500 nm wavelength in the fs-TA spectra (Fig. 5(a) and Fig. S23 in the ESM), corresponding to its ground-state bleach (GSB). The intense negative feature around 600 nm at 1 ps is caused by stimulated emission (SE), and it disappears after 2 ps due to the overlap with the positive signals in the same wavelength range. The positive feature between 500 and 700 nm is attributed to the excitation state absorption (ESA) of the holes of $BiVO_4$ [51, 52]. When the $BiVO_4$ is directly composited with TpPa-1 forming the TpPa-1/$BiVO_4$, a new intense GSB at 470 nm and the ESA at 510 nm appeared in the fs-TA spectra as shown in Fig. 5(b) and Fig. S24 in the ESM, which is assigned to the TpPa-1 component in the TpPa-1/$BiVO_4$. In contrast, for the Cu SAB photoanode of Cu_1-TpPa-1/$BiVO_4$, the fs-TA peak of SE shifts from 600 to 650 nm, as shown in Fig. 5(c) and Fig. S25 in the ESM, caused by the covalent interaction of $BiVO_4$ and TpPa-1 via the Cu single-atom bridge-bonds. Moreover, the GSB at 470 nm of TpPa-1 in the Cu_1-TpPa-1/$BiVO_4$ decreases significantly compared to that of TpPa-1/$BiVO_4$, caused by the photogenerated carriers trapping in $BiVO_4$ via the Cu SAB. The steady-state and transient photoluminescence (PL) measurements were further conducted to study photogenerated carrier combination for the prepared photoanodes. Figure S26(a) in the ESM shows that the steady-state PL intensity decreases most significantly for the Cu_1-TpPa-1/$BiVO_4$ photoanode compared to those of $BiVO_4$ and TpPa-1/$BiVO_4$ photoanodes. This indicates that the recombination of photogenerated carriers is effectively suppressed when the Cu single-atom is constructed between the $BiVO_4$ and TpPa-1. The transient PL lifetime in Fig. S26(b) in the ESM exhibits a lifetime of 5.8 ns for the Cu_1-TpPa-1/$BiVO_4$, longer than the 3.7 and 4.9 ns lifetimes of $BiVO_4$ and TpPa-1/$BiVO_4$, respectively. It confirms the slowest excitons recombination due to the enhanced charge separation in the Cu_1-TpPa-1/$BiVO_4$ photoanode.

To achieve an intuitive analysis of the photogenerated charge transfer performance in the prepared composite photoanodes, we employed *in-situ* Kelvin probe force microscopy (KPFM) to measure the surface potentials of the two composite photoanodes under illuminated and dark conditions. Figures 5(d)–5(f) display the surface potential of the TpPa-1/$BiVO_4$ before and after illumination, exhibiting an increase of over 40 mV upon illumination. Contrastively, as shown in Figs. 5(g)–5(i), the surface potential of Cu_1-TpPa-1/$BiVO_4$ photoanode significantly rises by approximately 163 mV under light excitation. These findings suggest that the SAB via the Cu-O_2N in the Cu_1-TpPa-1/$BiVO_4$ enhances hole transfer from the $BiVO_4$ to the outer Cu_1-TpPa-1 layer. Additionally, the separation and extraction of photogenerated charges are demonstrated using surface photovoltage (SPV) in Fig. S27 in the ESM. The spectral intensity of Cu_1-TpPa-1/$BiVO_4$ is notably stronger than that of bare $BiVO_4$ and TpPa-1/$BiVO_4$, particularly in the 450–525 nm range, confirming that the SAB of Cu atom can accelerate the separation of photogenerated hole/electron. This improvement is responsible for improving PEC water oxidation for oxygen evolution upon light excitation.

To further explain the better OER activity of Cu_1-TpPa-1/$BiVO_4$ photoanodes, the reaction pathway with the corresponding free energies, and the PDOS of reaction sites calculated by van der Waals corrected generalized gradient approximation (GGA)/Perdew–Burke–Ernzerhof for solids (PBESol) are plotted in Fig. 6. It should be noted that many COF materials without metal composition have been utilized as electrocatalysts or photocatalysts in water oxidation, in which the carbon sites in the COF were validated as active sites of OER [53–58]. In our work, for both Cu_1-TpPa-1/$BiVO_4$ model and TpPa-1/$BiVO_4$ model, the carbon site near central nitrogen atom in TpPa-1 is the reactive site. As shown in Figs. S28 and S29 in the ESM, *OH on carbon site is more stable (0.59 eV in total energy) than it on Cu site in Cu_1-TpPa-1/$BiVO_4$

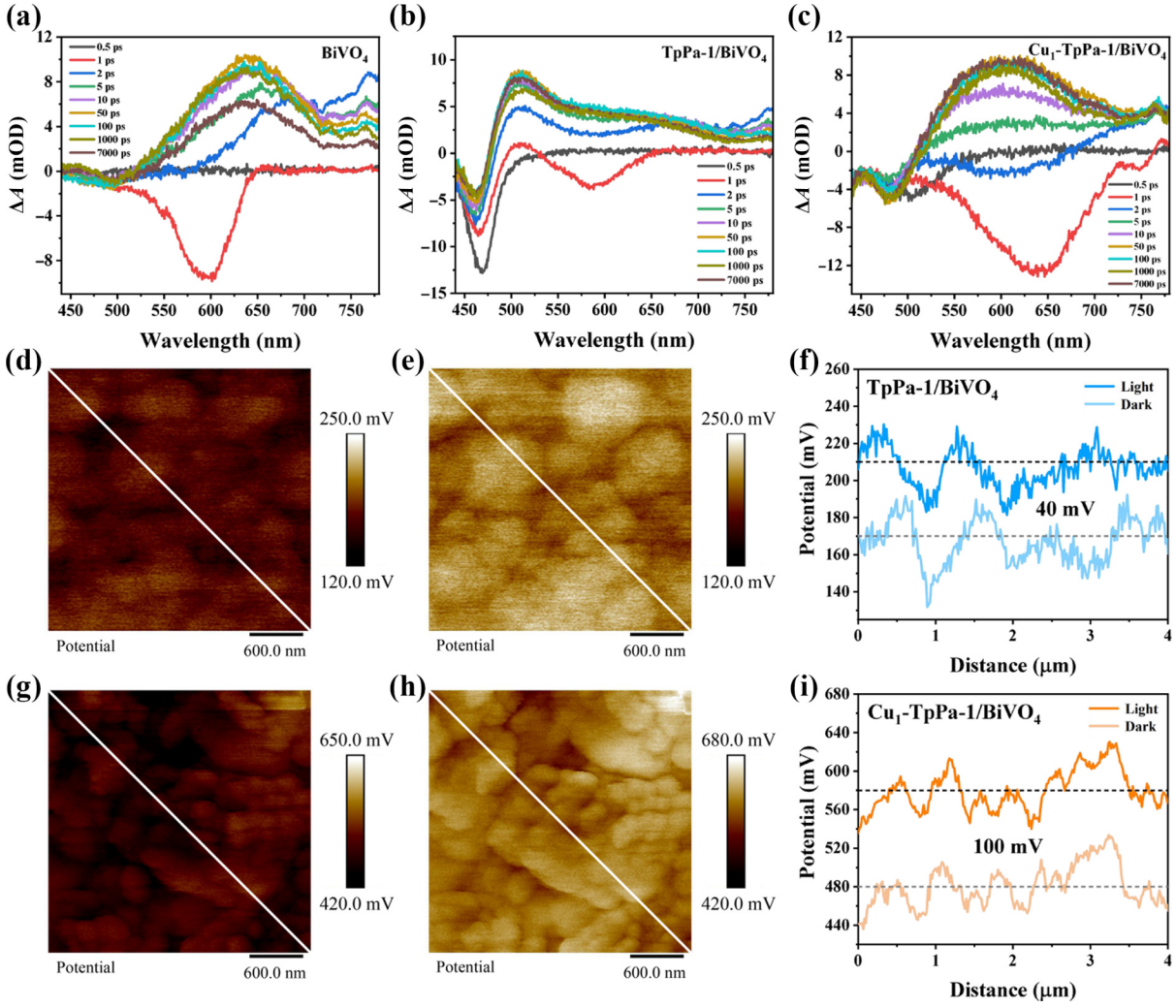

Figure 5 Femtosecond transient absorption spectra of (a) $BiVO_4$, (b) TpPa-1/$BiVO_4$, and (c) Cu_1-TpPa-1/$BiVO_4$. Kelvin probe force microscopy images of TpPa-1/$BiVO_4$ (d) in darkness and (e) under light irradiation. Kelvin probe force microscopy images of Cu_1-TpPa-1/$BiVO_4$ (g) in darkness and (h) under light irradiation. ((f) and (i)) The comparison of line-scanning surface potential under darkness and light irradiation.

model, indicating that Cu atom is not the preferable site to trigger OER [59]. Hence, combined with *in-situ* Raman experiments and charge injection efficiencies (Fig. S30 in the ESM), it was demonstrated that individual Cu atom does not contribute to the OER as a reactive center directly. Naturally, single Cu atom would tune the electronic properties of carbon reactive sites along Cu-N-C network. Due to their similarity, only OER intermediates (*OH, *O and *OOH) on Cu_1-TpPa-1/$BiVO_4$ model are shown in Fig. 6(a). The corresponding OER intermediates on TpPa-1/$BiVO_4$ model are shown in Fig. S31 in the ESM. The reaction Gibbs free energy diagrams of OER for both TpPa-1/$BiVO_4$ and Cu_1-TpPa-1/$BiVO_4$ models were calculated based on computational hydrogen electrode. As shown in Fig. 6(b), the formation of *OOH from *O in TpPa-1/$BiVO_4$ is the potential rate-determining step (RDS) with the overpotential (η) as high as 1.61 eV. After loading Cu single atoms, the η for the formation of *OOH from *O in Cu_1-TpPa-1/$BiVO_4$ reduced to 1.13 eV, which agrees well with the experimental results of LSV (Fig. S14 in the ESM). The PDOS of carbon reactive sites in both TpPa-1/$BiVO_4$ and Cu_1-TpPa-1/$BiVO_4$ models were also exhibited in Figs. 6(c) and 6(d), respectively. Obviously, it shows an intermediate energy band close to Fermi level (around −0.1 eV) in the p-band of carbon atom, which is mainly contributed by pz orbital for boosting the activity of carbon sites.

3 Conclusions

In summary, we developed a Cu-O_2N SAB at the interface of $BiVO_4$ and TpPa-1 photoanode. Experimental techniques of XAFS and XPS along with theoretical calculations demonstrate that the Cu single atoms form covalent bridge bonds by coordinating with O and N atoms in the COF and $BiVO_4$ via the coordination environment reconstruction. This SAB effectively enhances charge transfer and facilitates charge separation between $BiVO_4$ and TpPa-1 during PEC water oxidation. Consequently, the Cu_1-TpPa-1/$BiVO_4$ photoanode with the co-catalyst achieved a photocurrent density of 4.84 mA·cm^{-2} at 1.23 V vs. RHE as well as excellent stability in PEC SSW splitting. Further analysis demonstrated that the SAB introduces intermediate electronic energy states and reduces the energy gap of the O and N atoms across the bridge, establishing a channel for rapid charge transfer, and enhancing hole extraction from $BiVO_4$ semiconductors to TpPa-1. Overall, this study offers a promising strategy for designing highly efficient SAB photoelectrodes to improve PEC seawater oxidation performance,

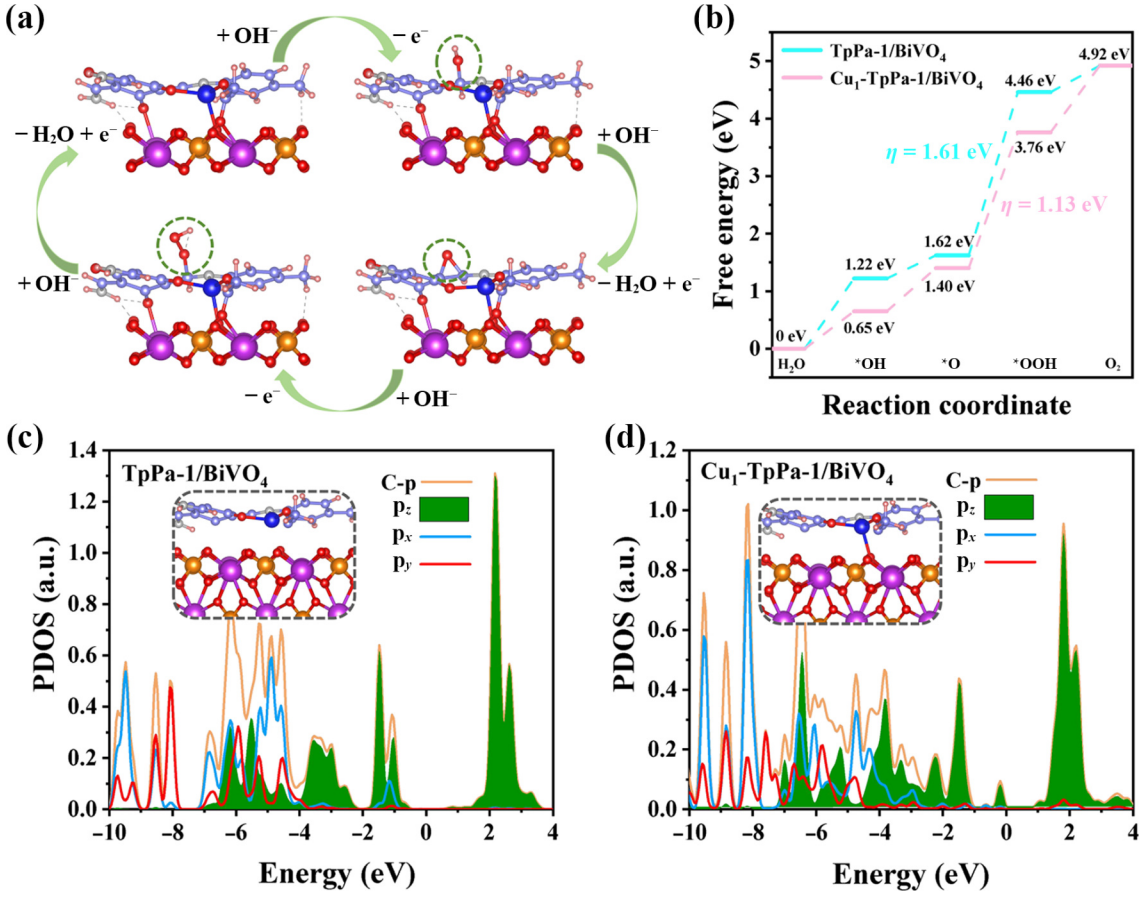

Figure 6 (a) Chemisorption model of Cu_1-TpPa-1/$BiVO_4$ for OER. (b) Calculated Gibbs free energy of TpPa-1/$BiVO_4$ and Cu_1-TpPa-1/$BiVO_4$ toward OER. ((c) and (d)) The PDOS of the active site of C in the TpPa-1/$BiVO_4$ and Cu_1-TpPa-1/$BiVO_4$, respectively.

while providing valuable insights into the fundamental mechanisms of charge transfer in PEC systems.

Electronic Supplementary Material: Supplementary material (preparation process of photoanodes, details of the characterization of photoanodes, PEC reaction device, and all calculation formulas) is available in the online version of this article at https://doi.org/10.26599/NR.2025.94907273.

Data availability

All data needed to support the conclusions in the paper are presented in the manuscript and the Electronic Supplementary Material. Additional data related to this paper may be requested from the corresponding author upon request.

Acknowledgements

This work was supported by the National Natural Science Foundation of China (Nos. 52172096 and 22375131). We thank the BL11B and BL14W1 stations in Shanghai Synchrotron Radiation Facility for the XAFS tests.

Declaration of competing interest

All the contributing authors report no conflict of interests in this work.

Author contribution statement

Z. C. Z.: Designed research, performed research, analyzed data, wrote the paper. G. H. S.: Analyzed data. W. M. S.: Analyzed data, wrote the paper. Z. R. H.: Analyzed data. Y. T.: Designed research, wrote the paper. All the authors have approved the final manuscript.

Use of AI statement

None.

References

[1] He, B.; Cao, Y.; Lin, K.; Wang, Y.; Li, Z.; Yang, Y. K.; Zhao, Y. L.; Liu, X. Q. Strong interactions between Au nanoparticles and $BiVO_4$ photoanode boosts hole extraction for photoelectrochemical water splitting. *Angew. Chem., Int. Ed.* **2024**, *63*, e202402435.

[2] Arunachalam, M.; Kanase, R. S.; Zhu, K.; Kang, S. H. Reliable bi-functional nickel-phosphate/TiO_2 integration enables stable n-GaAs photoanode for water oxidation under alkaline condition. *Nat. Commun.* **2023**, *14*, 5429.

[3] Wu, Z. L.; Liu, X. Y.; Li, H. J.; Sun, Z. Y.; Cao, M. S.; Li, Z. Z.; Fang, C. H.; Zhou, J. H.; Cao, C. B.; Dong, J. C. et al. A semiconductor-electrocatalyst nano interface constructed for successive photoelectrochemical water oxidation. *Nat. Commun.* **2023**, *14*, 2574.

[4] Liu, C. H.; Zhang, N. S.; Li, Y.; Fan, R. L.; Wang, W. J.; Feng, J. Y.; Liu, C.; Wang, J. O.; Hao, W. C.; Li, Z. S. et al. Long-term durability of metastable β-Fe_2O_3 photoanodes in highly corrosive seawater. *Nat.*

Commun. **2023**, *14*, 4266.

[5] Yang, J. W.; Ji, S. G.; Jeong, C. S.; Kim, J.; Kwon, H. R.; Lee, T. H.; Lee, S. A.; Cheon, W. S.; Lee, S.; Lee, H. et al. High-efficiency unbiased water splitting with photoanodes harnessing polycarbazole hole transport layers. *Energy Environ. Sci.* **2024**, *17*, 2541–2553.

[6] Wang, L. G.; Wu, J. B.; Wang, S. W.; Liu, H.; Wang, Y.; Wang, D. S. The reformation of catalyst: From a trial-and-error synthesis to rational design. *Nano Res.* **2024**, *17*, 3261–3301.

[7] Gao, R. T.; Guo, X. T.; Liu, S. J.; Zhang, X. Y.; Liu, X. H.; Su, Y. G.; Wang, L. Ultrastable and high-performance seawater-based photoelectrolysis system for solar hydrogen generation. *Appl. Catal. B: Environ.* **2022**, *304*, 120883.

[8] Ning, S. B.; Ou, H. H.; Li, Y. G.; Lv, C. C.; Wang, S. F.; Wang, D. S.; Ye, J. H. Co^{0}–$Co^{\delta+}$ interface double-site-mediated C–C coupling for the photothermal conversion of CO_2 into light olefins. *Angew. Chem., Int. Ed.* **2023**, *62*, e202302253.

[9] Song, J. J.; Wei, C.; Huang, Z. F.; Liu, C. T.; Zeng, L.; Wang, X.; Xu, Z. J. A review on fundamentals for designing oxygen evolution electrocatalysts. *Chem. Soc. Rev.* **2020**, *49*, 2196–2214.

[10] Liu, Y.; Zhang, Z. Y.; Wang, K.; Tan, X. L.; Chen, J. R.; Ren, X. L.; Jiang, F. Efficient $BiVO_4$ photoanode with an excellent hole transport layer of CuSCN for solar water oxidation. *Adv. Energy Mater.* **2024**, *14*, 2304223.

[11] Wang, J. M.; Xu, L.; Wang, T. X.; Li, R. J.; Zhang, Y. X.; Zhang, J.; Peng, T. Y. Porphyrin conjugated polymer grafted onto $BiVO_4$ nanosheets for efficient Z-scheme overall water splitting via cascade charge transfer and single-atom catalytic sites. *Adv. Energy Mater.* **2021**, *11*, 2003575.

[12] Gao, R. T.; Wang, L. Stable cocatalyst-free $BiVO_4$ photoanodes with passivated surface states for photocorrosion inhibition. *Angew. Chem., Int. Ed.* **2020**, *59*, 23094–23099.

[13] Gao, Y.; Yang, C. D.; Sun, F. L.; He, D. P.; Wang, X. Q.; Chen, J.; Zheng, X. B.; Liu, R. C.; Pan, H. G.; Wang, D. S. Ligand-tuning metallic sites in molecular complexes for efficient water oxidation. *Angew. Chem., Int. Ed.* **2025**, *64*, e202415755.

[14] Zhang, X. M.; Zhai, P. L.; Zhang, Y. X.; Wu, Y. Z.; Wang, C.; Ran, L.; Gao, J. F.; Li, Z. W.; Zhang, B.; Fan, Z. Z. et al. Engineering single-atomic Ni–N_4–O sites on semiconductor photoanodes for high-performance photoelectrochemical water splitting. *J. Am. Chem. Soc.* **2021**, *143*, 20657–20669.

[15] Gan, L.; He, G. S.; Liu, Y.; Li, W. Z.; Li, J. Engineering heteropolyblue hole transfer layer for efficient photoelectrochemical water splitting of $BiVO_4$ photoanodes. *Appl. Catal. B: Environ. Energy* **2024**, *349*, 123895.

[16] Wang, X. W.; Sun, W. M.; Tian, Y.; Dang, K.; Zhang, Q. M.; Shen, Z. R.; Zhan, S. H. Conjugated π electrons of MOFs drive charge separation at heterostructures interface for enhanced photoelectrochemical water oxidation. *Small* **2021**, *17*, 2100367.

[17] Zhang, Y. D.; Sun, Y. J.; Wang, Q. Y.; Zhuang, Z. C.; Ma, Z. T.; Liu, L. M.; Wang, G. M.; Wang, D. S.; Zheng, X. S. Synergy of photogenerated electrons and holes toward efficient photocatalytic urea synthesis from CO_2 and N_2. *Angew. Chem., Int. Ed.* **2024**, *63*, e202405637.

[18] Yang, N. C.; Zhang, S. N.; Xiao, Y. J.; Qi, Y.; Bao, Y. F.; Xu, P.; Jin, S. Y.; Zhang, F. X. Insight into the key restriction of $BiVO_4$ photoanodes prepared by pyrolysis method for scalable preparation. *Angew. Chem., Int. Ed.* **2023**, *62*, e202308729.

[19] Pei, H.; Peng, L. L.; Jiang, Z.; Zhang, Y. X.; Li, R. J.; Peng, T. Y. Gradient-tuned VO_4 vacancies in $BiVO_4$ photoanode for boosting bulk hole transport and oxygen evolution reaction performance. *Adv. Funct. Mater.* **2024**, *34*, 2401122.

[20] Gao, R. T.; Liu, S. J.; Guo, X. T.; Zhang, R. A.; He, J. L.; Liu, X. H.; Nakajima, T.; Zhang, X. Y.; Wang, L. Pt-induced defects curing on $BiVO_4$ photoanodes for near-threshold charge separation. *Adv. Energy Mater.* **2021**, *11*, 2102384.

[21] Sun, M.; Gao, R. T.; He, J. L.; Liu, X. H.; Nakajima, T.; Zhang, X. Y.; Wang, L. Photo-driven oxygen vacancies extends charge carrier lifetime for efficient solar water splitting. *Angew. Chem., Int. Ed.* **2021**, *60*, 17601–17607.

[22] Guo, X. T.; Liu, X. H.; Wang, L. $NiMoO_x$ as a highly protective layer against photocorrosion for solar seawater splitting. *J. Mater. Chem. A* **2022**, *10*, 1270–1277.

[23] Wang, G.; Wu, Y.; Li, Z. J.; Lou, Z. Z.; Chen, Q. Q.; Li, Y. F.; Wang, D. S.; Mao, J. J. Engineering a copper single-atom electron bridge to achieve efficient photocatalytic CO_2 conversion. *Angew. Chem., Int. Ed.* **2023**, *62*, e202218460.

[24] Zhang, Y. L.; Liu, B.; Dai, Y. K.; Shen, L. X.; Guo, P.; Xia, Y. F.; Zhang, Z. Y.; Kong, F. T.; Zhao, L.; Wang, Z. B. Engineering Co–N–Cr cross-interfacial electron bridges to break activity-stability trade-off for superdurable bifunctional single atom oxygen electrocatalysts. *Angew. Chem., Int. Ed.* **2024**, *63*, e202400577.

[25] Gan, T.; Wang, D. S. Atomically dispersed materials: Ideal catalysts in atomic era. *Nano Res.* **2024**, *17*, 18–38.

[26] Ou, H. H.; Qian, Y. P.; Yuan, L. T.; Li, H.; Zhang, L. D.; Chen, S. H.; Zhou, M.; Yang, G. D.; Wang, D. S.; Wang, Y. G. Spatial position regulation of Cu single atom site realizes efficient nanozyme photocatalytic bactericidal activity. *Adv. Mater.* **2023**, *35*, 2305077.

[27] Wang, Y.; Ma, F. Y.; Zhang, G. Q.; Zhang, J. W.; Zhao, H.; Dong, Y. M.; Wang, D. S. Precise synthesis of dual atom sites for electrocatalysis. *Nano Res.* **2024**, *17*, 9397–9427.

[28] Tao, Y.; Guan, J. P.; Zhang, J.; Hu, S. Y.; Ma, R. Z.; Zheng, H. R.; Gong, J. X.; Zhuang, Z. C.; Liu, S. J.; Ou, H. H. et al. Ruthenium single atomic sites surrounding the support pit with exceptional photocatalytic activity. *Angew. Chem., Int. Ed.* **2024**, *63*, e202400625.

[29] Li, J.; Zhou, J.; Wang, X. H.; Guo, C.; Li, R. H.; Zhuang, H. F.; Feng, W. H.; Hua, Y. J.; Lan, Y. Q. *In situ* construction of single-atom electronic bridge on COF to enhance photocatalytic H_2 production. *Angew. Chem. , Int. Ed.* **2024**, *63*, e202411721.

[30] Tang, H. T.; Zhou, H. Y.; Pan, Y. M.; Zhang, J. L.; Cui, F. H.; Li, W. H.; Wang, D. S. Single-atom manganese-catalyzed oxygen evolution drives the electrochemical oxidation of silane to silanol. *Angew. Chem., Int. Ed.* **2024**, *63*, e202315032.

[31] Guo, Y. J.; Liu, Z. Y.; Zhou, D. Y.; Zhang, M. Y.; Zhang, Y.; Li, R. Z.; Liu, S. L.; Wang, D. S.; Dai, Z. H. Competition and synergistic effects of Ru-based single-atom and cluster catalysts in electrocatalytic reactions. *Sci. China Mater.* **2024**, *67*, 1706–1720.

[32] Mu, X. Q.; Zhang, X. Y.; Chen, Z. Y.; Gao, Y.; Yu, M.; Chen, D.; Pan, H. Z.; Liu, S. L.; Wang, D. S.; Mu, S. C. Constructing symmetry-mismatched $Ru_xFe_{3-x}O_4$ heterointerface-supported Ru clusters for efficient hydrogen evolution and oxidation reactions. *Nano Lett.* **2024**, *24*, 1015–1023.

[33] Mu, X. Q.; Yu, M.; Liu, X. Y.; Liao, Y. R.; Chen, F. J.; Pan, H. Z.; Chen, Z. Y.; Liu, S. L.; Wang, D. S.; Mu, S. C. High-entropy ultrathin amorphous metal-organic framework-stabilized Ru(Mo) dual-atom sites for water oxidation. *ACS Energy Lett.* **2024**, *9*, 5763–5770.

[34] Zhang, H. L.; Lin, Z.; Kidkhunthod, P.; Guo, J. Stable immobilization of nickel ions on covalent organic frameworks for panchromatic photocatalytic hydrogen evolution. *Angew. Chem., Int. Ed.* **2023**, *62*, e202217527.

[35] Qiu, J. Y.; Meng, K.; Zhang, Y.; Cheng, B.; Zhang, J. J.; Wang, L. X.; Yu, J. G. COF/In_2S_3 S-scheme photocatalyst with enhanced light absorption and H_2O_2-production activity and fs-TA investigation. *Adv. Mater.* **2024**, *36*, 2400288.

[36] Wang, L. N.; Zhang, J. M.; Li, Y.; Shi, Y. B.; Huang, J. W.; Mei, Q.; Wang, L.; Ding, F.; Bai, B.; Wang, Q. Z. Heterostructured $CoFe_{1.5}Cr_{0.5}S_3O$/COFs/$BiVO_4$ photoanode boosts charge extraction for efficient photoelectrochemical water splitting. *Appl. Catal. B: Environ.* **2023**, *336*, 122921.

[37] Dong, P. Y.; Wang, Y.; Zhang, A. C. J.; Cheng, T.; Xi, X. G.; Zhang, J. L. Platinum single atoms anchored on a covalent organic

framework: Boosting active sites for photocatalytic hydrogen evolution. *ACS Catal.* **2021**, *11*, 13266–13279.
[38] Weng, W. J.; Guo, J. The effect of enantioselective chiral covalent organic frameworks and cysteine sacrificial donors on photocatalytic hydrogen evolution. *Nat. Commun.* **2022**, *13*, 5768.
[39] Li, Z. W.; Shi, X. R.; Cheng, H. J.; Song, Y. R.; Jiao, Y. Y.; Shi, S. B.; Gao, J. F.; Hou, J. G. Atomically dispersed iron active sites on covalent organic frameworks for artificial photosynthesis of hydrogen peroxide. *Adv. Energy Mater.* **2024**, *14*, 2302797.
[40] Wang, G. B.; Wang, Y. J.; Kan, J. L.; Xie, K. H.; Xu, H. P.; Zhao, F.; Wang, M. C.; Geng, Y.; Dong, Y. B. Construction of covalent organic frameworks via a visible-light-activated photocatalytic multicomponent reaction. *J. Am. Chem. Soc.* **2023**, *145*, 4951–4956.
[41] Ran, L.; Li, Z. W.; Ran, B.; Cao, J. Q.; Zhao, Y.; Shao, T.; Song, Y. R.; Leung, M. K. H.; Sun, L. C.; Hou, J. G. Engineering single-atom active sites on covalent organic frameworks for boosting CO_2 photoreduction. *J. Am. Chem. Soc.* **2022**, *144*, 17097–17109.
[42] Lin, C.; Shan, Z.; Dong, C. R.; Lu, Y.; Meng, W. K.; Zhang, G.; Cai, B.; Su, G. Y.; Park, J. H.; Zhang, K. Covalent organic frameworks bearing Ni active sites for free radical-mediated photoelectrochemical organic transformations. *Sci. Adv.* **2023**, *9*, eadi9442.
[43] Biswal, B. P.; Chandra, S.; Kandambeth, S.; Lukose, B.; Heine, T.; Banerjee, R. Mechanochemical synthesis of chemically stable isoreticular covalent organic frameworks. *J. Am. Chem. Soc.* **2013**, *135*, 5328–5331.
[44] Yang, J.; Deng, C. Y.; Lei, Y.; Duan, M. Y.; Yang, Y. S.; Chen, X. R.; Yang, S. P.; Li, J. K.; Sheng, H.; Shi, W. Q. et al. Fe–N Co-doped $BiVO_4$ photoanode with record photocurrent for water oxidation. *Angew. Chem., Int. Ed.* **2025**, *64*, e202416340.
[45] Wang, H.; Gao, R. T.; Nguyen, N. T.; Bai, J. W.; Ren, S. J.; Liu, X. H.; Zhang, X. Y.; Wang, L. Superhydrophilic CoFe dispersion of hydrogel electrocatalysts for quasi-solid-state photoelectrochemical water splitting. *ACS Nano* **2023**, *17*, 22071–22081.
[46] Xu, M. L.; Lu, M.; Qin, G. Y.; Wu, X. M.; Yu, T.; Zhang, L. N.; Li, K.; Cheng, X.; Lan, Y. Q. Piezo-photocatalytic synergy in $BiFeO_3$@COF Z-scheme heterostructures for high-efficiency overall water splitting. *Angew. Chem., Int. Ed.* **2022**, *61*, e202210700.
[47] Yang, Y. L.; Wang, Y. R.; Dong, L. Z.; Li, Q.; Zhang, L.; Zhou, J.; Sun, S. N.; Ding, H. M.; Chen, Y. F.; Li, S. L. et al. A honeycomb-like porous crystalline hetero-electrocatalyst for efficient electrocatalytic CO_2 reduction. *Adv. Mater.* **2022**, *34*, 2206706.
[48] Wu, W. L.; Wang, Y. N.; Luo, L.; Wang, M. L.; Li, Z. L.; Chen, Y.; Wang, Z. Q.; Chai, J. B.; Cen, Z. Y.; Shi, Y. L. et al. CO_2 hydrogenation over copper/ZnO single-atom catalysts: Water-promoted transient synthesis of methanol. *Angew. Chem. , Int. Ed.* **2022**, *61*, e202213024.
[49] He, T.; Zhao, Z. F.; Liu, R. Y.; Liu, X. Y.; Ni, B.; Wei, Y. P.; Wu, Y. L.; Yuan, W.; Peng, H. J.; Jiang, Z. Y. et al. Porphyrin-based covalent organic frameworks anchoring au single atoms for photocatalytic nitrogen fixation. *J. Am. Chem. Soc.* **2023**, *145*, 6057–6066.
[50] Sun, L.; Zhang, Z. Q.; Bian, J.; Bai, F. Q.; Su, H. W.; Li, Z. J.; Xie, J. J.; Xu, R. P.; Sun, J. H.; Bai, L. L. et al. A Z-scheme heterojunctional photocatalyst engineered with spatially separated dual redox sites for selective CO_2 reduction with water: Insight by *in situ* μs-transient absorption spectra. *Adv. Mater.* **2023**, *35*, 2300064.
[51] Deng, Y. T.; Zhou, H. P.; Zhao, Y.; Yang, B.; Shi, M.; Tao, X. P.; Yang, S. Q.; Li, R. G.; Li, C. Spatial separation of photogenerated charges on well-defined bismuth vanadate square nanocrystals. *Small* **2022**, *18*, 2103245.
[52] Ravensbergen, J.; Abdi, F. F.; van Santen, J. H.; Frese, R. N.; Dam, B.; van de Krol, R.; Kennis, J. T. M. Unraveling the carrier dynamics of $BiVO_4$: A femtosecond to microsecond transient absorption study. *J. Phys. Chem. C* **2014**, *118*, 27793–27800.
[53] Mondal, S.; Mohanty, B.; Nurhuda, M.; Dalapati, S.; Jana, R.; Addicoat, M.; Datta, A.; Jena, B. K.; Bhaumik, A. A thiadiazole-based covalent organic framework: A metal-free electrocatalyst toward oxygen evolution reaction. *ACS Catal.* **2020**, *10*, 5623–5630.
[54] Yang, C. H.; Yang, Z. D.; Dong, H.; Sun, N.; Lu, Y.; Zhang, F. M.; Zhang, G. L. Theory-driven design and targeting synthesis of a highly-conjugated basal-plane 2D covalent organic framework for metal-free electrocatalytic OER. *ACS Energy Lett.* **2019**, *4*, 2251–2258.
[55] Wang, R.; Zhang, Z. Q.; Suo, J. Q.; Liao, L.; Li, L. B.; Yu, Z. C.; Zhang, H.; Valtchev, V.; Qiu, S. L.; Fang, Q. R. Exploring metal-free ionic covalent organic framework nanosheets as efficient OER electrocatalysts via cationic–π interactions. *Chem. Eng. J.* **2023**, *478*, 147403.
[56] Yang, Y.; Chu, X. Y.; Zhang, H. Y.; Zhang, R.; Liu, Y. H.; Zhang, F. M.; Lu, M.; Yang, Z. D.; Lan, Y. Q. Engineering *β*-ketoamine covalent organic frameworks for photocatalytic overall water splitting. *Nat. Commun.* **2023**, *14*, 593.
[57] Wan, Y. Y.; Wang, L.; Xu, H. X.; Wu, X. J.; Yang, J. L. A simple molecular design strategy for two-dimensional covalent organic framework capable of visible-light-driven water splitting. *J. Am. Chem. Soc.* **2020**, *142*, 4508–4516.
[58] Lin, C. Y.; Zhang, L. P.; Zhao, Z. H.; Xia, Z. H. Design principles for covalent organic frameworks as efficient electrocatalysts in clean energy conversion and green oxidizer production. *Adv. Mater.* **2017**, *29*, 1606635.
[59] Mu, X. Q.; Liu, S. L.; Zhang, M. Y.; Zhuang, Z. C.; Chen, D.; Liao, Y. R.; Zhao, H. Y.; Mu, S. C.; Wang, D. S.; Dai, Z. H. Symmetry-broken Ru nanoparticles with parasitic Ru–Co dual-single atoms overcome the volmer step of alkaline hydrogen oxidation. *Angew. Chem., Int. Ed.* **2024**, *63*, e202319618.